1   **Comparing the Fate of Brain Metastatic Breast Cancer Cells in Different Immune Compromised Mice with**

2   **Cellular Magnetic Resonance Imaging**

3

4   Natasha N. Knier[1,2], Amanda M. Hamilton[1], and Paula J. Foster[1,2]

5

6   [1]Imaging Research Laboratories, Robarts Research Institute, London, ON, Canada

7   [2]Department of Medical Biophysics, Western University, London, ON, Canada

8

9

10

11

12   Address correspondence to:

13   Natasha N. Knier

14   Robarts Research Institute,

15   Schulich School of Medicine and Dentistry,

16   Western University

17   London, Ontario, N6A 5B7,

18   Canada

19   Email: nknier@uwo.ca

20

21

24

1

Abstract

Metastasis is the leading cause of mortality in breast cancer patients, with brain metastases becoming increasingly prevalent. Studying this disease is challenging due to the limited experimental models and methods available. Here, we used iron-based cellular MRI to track the fate of a mammary carcinoma cell line (MDA-MB-231-BR) *in vivo* to characterize the growth of brain metastases in the nude and severely immune-compromised NOD/SCID/ILIIrg-/- (NSG) mouse.

Nude and NSG mice received injections of iron-labeled MDA-MB-231-BR cells. Images were acquired with a 3T MR system and assessed for signal voids and metastases. The percentage of signal voids and the number and volume of metastases were quantified. *Ex vivo* imaging of the liver, histology, and immunofluorescence labeling was performed.

On day 0, iron-labeled cells were visualized as signal voids throughout the brain. The percentage of voids decreased significantly between day 0 and endpoint. At endpoint, there was no difference in the number of brain metastases or tumour burden in NSG mice compared to nudes. Tumour volumes in nude mice were significantly larger than in NSG mice. Body images indicated that the NSG mice had metastases in the liver, lungs, and lymph nodes.

Characterization of the NSG and nude mouse is necessary to study breast cancer brain metastasis *in vivo*. Here, we show that the 231BR cell line grew differently in NSG mice compared to nude mice. This work demonstrates the role that imaging can play toward credentialing these models that cannot be done with other *in vitro* or histopathologic methods alone.

Background

Breast cancer is a leading cause of death in women mainly due to the propensity of breast tumors to metastasize to regional and distant sites, such as the lymph node, lung, liver, bone and brain [1]. The incidence of brain metastases is increasing due to the introduction of more sensitive diagnostic methods and improved systemic therapies leading to improvements in extra-cranial control and survival [2-4]. Breast cancer is a disease with a number of subtypes and patients with metastatic 'triple-negative' breast cancer tend to develop brain metastasis at a high rate [5, 6]. For the HER2 amplified subtype, the frequency of brain metastasis has been reported to be as high as 50% [7].

Once a metastatic cancer cell arrives in the brain one of three things can happen: (1) it may die, (2) it may proliferate to form micrometastases, or (3) it may remain viable but dormant ('non-proliferative') [8, 9] If the solitary cells proliferate to form micrometastases, they may again experience one of three fates: (1) they may die, (2) they may continue to proliferate and form macrometastases, or (3) they may persist as "dormant" micrometastases, where dormancy is defined as a balance between proliferation and apoptosis within the cell population such that there is no net growth [9, 10]. The factors that tip the balance between dormancy and proliferation are poorly understood. Both dormant single cells and dormant micrometastases are believed to be sources of cells that contribute to tumor recurrence [11]. Dormant cancer cells also present a substantial therapeutic problem; since they are quiescent, they are non-responsive to current therapies which target proliferating cells [8].

Currently, only a handful of models specific to breast cancer brain metastasis have been described and even fewer allow for *in vivo* investigation of cancer cell dormancy. Both murine and human cancer cell lines have been developed to mimic as many steps in the metastatic cascade as possible. A well characterized murine breast cancer cell line is the 4T1-BR5 cell line, a highly tumorigenic and invasive cell line that has undergone multiple rounds of selection to preferentially grow in the mouse brain [12]. There are several advantages to using a murine breast cancer cell line to study brain metastasis, as growth and maintenance is easy and relatively inexpensive, and it can be grown in immune-competent mice, which is of particular interest for studying this disease in a way that recapitulates the tumor microenvironment [13].

71   A small number of human breast cancer brain metastatic cell lines have also been developed, including the

72   commonly used MDA-MB-231BR (231BR), MDA-MB-231BR-HER2, MA11, JIMT1-BR3, SUM190-BR3 cell

73   lines. The MDA-MB-231BR cell line has been particularly well characterized for studying the progression of brain

74   metastases in nude mice. Nude mice are the most commonly used immune-deficient strain for models which use

75   human cell lines. They have a genetic mutation that causes a deteriorated or absent thymus, resulting in a lack of T

76   cells [14]. The 231BR cell line grows selectively in the brain of nude mice, without metastatic growth seen in other

77   distant organs [15]. Human breast cancer cell lines are one of the most widely used models to study the metastatic

78   growth of cancer *in vitro* and *in vivo*, as they have been used to provide extensive insight into the characteristics of

79   human cells and can be used for high throughput screening of various drugs [16]. There are, however, significant

80   limitations to using human and murine breast cancer cell lines, as the quick progression *in vivo* can limit

81   opportunities for adequate therapeutic testing, and the growth of these cells *in vitro* prior to establishment in a mouse

82   can cause changes in the genetic composition due to clonal selection [17]. Many groups have shown that these

83   genetic changes result in these models failing to maintain tumor heterogeneity, which is now recognized as a critical

84   element for developing personalized treatments [18-20]. Studying breast cancer with immunocompetent mice also

85   has limitations, as tumor latency and growth can be variable and slow [21]. There is also increased difficulty in

86   establishing human tumors successfully in these mice. Immune-compromised mice lack a comparable tumor

87   microenvironment to clinical tumors and fail to provide a realistic result of interactions with the natural immune

88   response, particularly in the case of studying anticancer therapeutics [22].

89

90   In more recent years, researchers have moved towards studying breast cancer and its subtypes with patient-derived

91   xenografts (PDX), which allow for the growth of human primary breast cancer tissue that has been recently resected

92   from consenting patients into immune-compromised rodents [23]. NOD/SCID/ILIIrg$^{-/-}$ (NSG) mice are the preferred

93   strain of mice to engraft a PDX, as they are highly permissive to growing breast cancer metastasis, and resembles

94   the metastatic pattern seen in human patients. NSG mice are the most immunodeficient mouse strains to date,

95   lacking T cells, B cells, NK cells, and have defective macrophages and dendritic cells [24-26]. Even fewer PDX

96   models have been developed specific to breast cancer brain metastasis, including the novel F2-7 and E22-1 PDX cell

97   lines [27], as well as others who have established low passage PDX models of breast cancer brain metastasis and

98   those that implant fresh tumor tissue directly into the rodent brain [28].

4

99   The D2.0R and related D2A1 mouse mammary tumor cells have been well characterized as model systems for

100   tumor cell dormancy. In mice, D2.0R/R cells invade distant metastatic sites, remain as single quiescent cells for

101   prolonged periods of time, and occasionally proliferate into metastatic tumors. D2A1/R cells, have a much shorter

102   dormancy period before forming metastases in the lung, liver, and other organs [29]. A human breast cancer cell

103   line, MCF-7 has also been studied to examine the mechanisms of dormancy, however it is poorly metastatic [30].

104   For all of these brain metastasis models – cancer cell growth, metastasis and dormancy are typically studied using

105   methods such as histology, flow cytometry, immunohistochemistry, and fluorescent microscopy [31]. While these

106   techniques provide useful information about molecular and cellular markers and morphology, they are limited to

107   studying this disease after endpoint has been reached. There is a clear need to characterize brain metastatic models

108   of breast cancer *in vivo*, which can be accomplished through use of imaging modalities and cell tracking techniques.

109

110   Cellular magnetic resonance imaging (MRI) combines the ability to obtain high resolution MRI data with the use of

111   iron oxide nanoparticles for labeling specific cells, thereby enhancing their detectability [32, 33]. The presence of

112   the iron in cells causes a distortion in the magnetic field and leads to abnormal signal hypo-intensities in iron-

113   sensitive images (T2*-weighted images are most often used). Areas containing iron labeled cells therefore appear as

114   regions of low signal intensity on MRI images, creating negative contrast [34]. We have previously shown that it is

115   possible to use cellular MRI to track iron-labeled 231BR cancer cells in the nude mouse brain [35-37]. Proliferative

116   cancer cells lose the iron label over time; as the cells divide the particles are apportioned to daughter cells and

117   eventually some cells contain too little iron to be detectable by MRI. As brain metastases form, changes to the tissue

118   result in the tumor appearing brighter than the surrounding brain in MRI. Nonproliferative cancer cells retain the

119   iron particles and can be detected over long periods of time [37].

120

121   In this study, we used these cellular MRI techniques to characterize and compare the growth of 231BR brain

122   metastases and the persistence of iron-retaining cancer cells in nude and NSG mice. Our goal was to evaluate the

123   NSG mouse as a model for breast cancer brain metastasis and dormancy.

124

125   **Methods**

126   **Cell Culture and MPIO Labeling Procedure**

127   Brain trophic human breast cancer cells (MDA-MB-231BR) expressing green fluorescent protein (GFP) were

128   maintained with Dulbecco's modified Eagle's medium containing 10% fetal bovine serum (complete DMEM) at

129    $37°C$ and 5% CO_2. $2x10^6$ of these cells were seeded and allowed to adhere for 24 hours. To iron label these cells,

130   cells were supplemented with 25 μg Fe/mL of micron-sized iron oxide particles (MPIO) (0.9 μm diameter, ~63%

131   magnetite, labeled with Flash Red; Bangs Laboratory, Fishers, IN, USA) in 10mL of complete DMEM in a T75-cm^2

132   flask. Following this, cells were washed once with phosphate buffered solution (PBS) within the flask and

133   trypsinized with 0.25% Trypsin-EDTA. After, cells were harvested and washed three additional times with PBS in

134   the flask to thoroughly remove unincorporated MPIO prior to cell injections. Cell viability was assessed and

135   calculated using the Trypan blue exclusion assay. To visualize MPIO labelling, labeled cells were affixed to a glass

136   slide with a ThermoFisher Cytospin 4 cytocentrifuge and fixed with a Methanol/Acetic acid solution. Slides were

137   then stained with a Perl's Prussian Blue (PPB) solution and counterstained with Nuclear Fast Red. Slides were

138   dehydrated with increasing concentrations of ethanol, cleared with xylene, and coverslipped with a xylene-based

139   mounting medium. These PPB-stained slides were examined to assess the localization of MPIO within the cell and

140   to determine the labeling efficiency using a Zeiss AXIO Imager A1 Microscope (Zeiss Canada, Toronto, ON,

141   Canada). Iron oxide nanoparticles appear dark blue, and cells appear light pink in colour.

142

143   **Animal Model and Work Flow**

144   All animals were cared for in accordance with the standards of the Canadian Council on Animal Care, under an

145   approved protocol of the University of Western Ontario's Council on Animal Care and housed in a pathogen-free

146   barrier facility. Female nude mice (nu/nu Foxn1, aged 6-8 weeks, from Charles River Laboratories, Wilmington,

147   MA) and female NSG mice (NOD.Cg-$Prkdc^{scid}Il2rg^{tm1Wjl}$/SzJ, 6-8 weeks, Humanized Mouse and

148   Xenotransplantation Facility, Robarts Research Institute, University of Western Ontario, London, ON) were first

149   anesthetized with isoflurane (2% in 100% oxygen). Nude (n=10) and NSG mice (n=10) were then injected with a

150   suspension of $1.5x10^5$ MPIO-labeled MDA-MB-231BR/GFP+ cells in 100μL of sterile saline and 15% Vevo

151   MicroMarker microbubble solution (FUJIFILM, VisualSonics Inc., Toronto, ON, Canada). Cell suspension was

152   loaded into a 100μL Hamilton syringe with a 30G needle. Cells were administered by slow intracardiac injection

153   into the beating left ventricle of the heart with ultrasound imaging guidance on a Vevo 2100 ultrasound system

154   (FUJIFILM, VisualSonics Inc., Toronto, ON, Canada). Cancer cell arrest was evaluated with MRI on the day of the

6

155 injection (Day 0) and used to determine whether mice had a successful intracardiac injection. Absence of signal

156 voids in the brain indicated an unsuccessful injection, resulting in exclusion from the remainder of the study. Nude

157 mice with successful injections had MRI performed at day 21 and day 32 post-injection. NSG mice with successful

158 injections had MRI performed at day 21 post-injection (Figure 1).

159 Additionally, 1 nude mouse and 3 NSG mice received intracardiac injections with 1.5×10^5 MPIO labeled MD-MB-

160 231BR/GFP+ cells and intraperitoneal injections of 200μL of gadopentetate dimeglumine (Magnevist, Schering,

161 US; 0.5 mmol/mL) on Day 0 to assess cancer cell arrest in the liver. These mice were sacrificed on Day 0 by

162 isoflurane overdose approximately 40 minutes after intraperitoneal administration. These mice were then

163 exsanguinated, and brains and livers were removed for *ex vivo* imaging.

164

165 **Magnetic Resonance Imaging**

166 All brain and body MRI examinations were acquired on a 3.0 Tesla GE MR750 clinical MR scanner (General

167 Electric, Mississauga, ON, Canada) using a custom-built gradient coil (inner diameter = 17.5 cm, gradient strength =

168 500 mT/m, and peak slew rate = 3000 T/m/s]). Brain and ex vivo liver images used a custom-built solenoidal mouse

169 brain radiofrequency (RF) coil. Body images were acquired using a 4.3 x 4.3 cm dual tuned ^{1}H/^{19}F surface coil

170 (Clinical MR Solutions, WI, USA), originally built for imaging small ROIs in humans. Mice were anesthetized with

171 2% isoflurane in 100% oxygen administered through a nose cone. *In vivo* brain and body images were acquired

172 using a 3D balanced steady-state free precession (bSSFP) sequence [Fast Imaging Employing Steady State

173 Acquisition (FIESTA) on a GE system] that has been optimized for simultaneous detection of signal voids produced

174 by iron-loaded cells and hyperintense metastases. This permitted the assessment of both cell arrest and retention as

175 well as the number and volume of metastases throughout the mouse brain. Brain images for nude mice were

176 acquired on day 0, day 21, and day 32. Brain imaging for NSG mice occurred on day 0 and day 21. Scanning

177 parameters were as follows: resolution = 100 x 100 x 200 μm, repetition time (TR) = 7 ms, echo time (TE) = 3.5 ms,

178 bandwidth (BW) = 20.83kHz, flip angle (FA) = 35 degrees, signal averages = 2, phase cycles = 8, matrix = 150 x

179 150, scan time = approximately 33 minutes per mouse. Body images were acquired on Day 20. Body imaging

180 parameters were as follows: resolution = 200 x 200 x 200 μm, repetition time (TR) = 4.7 ms, echo time (TE) = 2.3,

181 bandwidth (BW) = +/-31.25 kHZ, flip angle (FA) = 35 degrees, signal averages = 2, phase cycles = 8, matrix = 250

182 x 250, scan time = approximately 20 minutes. *Ex vivo* liver imaging parameters were acquired using a spoiled

7

183   gradient echo sequence that also allows for the detection of signal voids throughout the liver. *Ex vivo* liver samples

184   were immersed in tubes containing Fluorinert™ FC-40 Electronic Liquid (3M, St. Paul's, MN, USA), a

185   fluorocarbon liquid which produces a black background in proton images. Images were taken of ex vivo livers

186   acquired on day 0 for both strains, day 21 for the NSG mouse, and day 32 for the nude mouse. The scanning

187   parameters for ex vivo liver images were as follows: resolution = 100 x 100 x 200 um, repetition time (TR) = 43 ms,

188   echo time (TE) 4.844 ms, bandwidth (BW) = 31.25kHz, flip angle (FA) = 60 degrees, signal averages = 1, phase

189   cycles = 8, matrix = 250 x 250, scan time = approximately 23 minutes.

190

191   **Image Analysis**

192   Images were analyzed using open-source OsiriX image software (Pixmeo, SARL, Bernex, Switzerland), version

193   10.0.4 and Horos image software, version 3.3.5. Brain images were evaluated for successful cell delivery by

194   assessment of signal voids on day 0. To quantify cancer cell arrest throughout the brain, the number of black pixels

195   within the total brain volume was determined from day 0 MRI images. The brain was manually segmented as a

196   region of interest and then a threshold value was determined based on the mean pixel intensity value of a

197   representative signal void within the brain region ± 2 standard deviations. The total number of black pixels under

198   this threshold value within the entire brain volume signal was obtained from a pixel intensity histogram. To quantify

199   brain metastases at day 21 and day 32, tumors were counted in all image slices by a single observer. Each tumor was

200   manually segmented, and the tumor volumes were reconstructed using the OsiriX and Horos volume algorithm. To

201   calculate brain tumor burden at day 21 and day 32, an ROI was drawn around the outline of the brain in each slice,

202   and a 3D reconstruction using the OsiriX and Horos volume algorithm provided a quantification of the total brain

203   volume. The total volume of all segmented tumors was then determined by adding each individual tumor volume

204   measurement and calculating the percentage of the total brain volume occupied by tumors. Body images were

205   qualitatively assessed for the presence of metastases in the liver, lung, and lymph nodes. All quantitative values

206   were presented as the mean ± standard error. Statistical analysis was performed using Welch's *t* tests on GraphPad

207   Prism version 8 software (GraphPad, San Diego, CA).

208

209   **Histology and Immunohistochemistry**

210 At each strain's respective endpoints, mice were euthanized by isofluorane overdose and perfused with 4%

211 paraformaldehyde. Brains were removed and placed into paraformaldehyde for another 24 hours. Fixed brains were

212 processed, paraffin embedded and then cut into 6 or 8 um sections. Sliced sections were deparaffinized and stained

213 with either hematoxylin and eosin (H&E) or immunofluorescently labelled for Ki67.

214

215 **Hematoxylin and eosin (H&E) staining**

216 Sections were washed briefly in distilled water, stained in Harris hematoxylin solution for 5 minutes and

217 differentiated in 1% acid alcohol for 30 seconds. After washing in 0.2% ammonia for 5 minutes, sections were

218 counterstained in eosin-phloxine solution for 30 seconds; dehydrated through 95% alcohol, 2 changes of absolute

219 alcohol, and 5 minutes each. Sections were then dehydrated and cleared through 95% ethyl alcohol, absolute alcohol

220 and xylene, and mounted with resinous medium.

221

222 **Immunofluorescent labelling**

223 Ki-67 immunostaining was performed using a rat anti-Ki-67 antibody (1:400 dilution; Catalog #14-5698-82,

224 Invitrogen). All sections were permeabilized with 0.2% Triton X-100 in PBS for 15 minutes and non-specific

225 protein binding was then blocked by incubation in a commercial blocking agent (ab156024, Abcam) for 1 hour at

226 room temperature. Sections were then incubated with the Ki-67 primary antibody in commercial antibody dilutant

227 (ab64211, Abcam) at room temperature for 1 hour. Negative controls (without addition of primary antibody) were

228 performed on adjacent sections. Unbound primary antibody was washed away through three 5-minute exchanges of

229 1xPBS. Sections were then incubated with an anti-rat Alexa Fluor-488 secondary antibody (1:300 dilution; Catalog

230 #A-11006, Invitrogen) for 1 hour. Unbound secondary antibody was washed away through three 5-minute

231 exchanges of 1xPBS. Finally, nuclei were counterstained with Hoechst 33258 for 5 minutes and rinsed sections

232 cover slipped for microscopic examination.

233

234 **Results**

235 *In Vitro* **Studies**

236 *Cell Labelling*

237   MDA-MB-231BR cells were efficiently labeled with MPIO, as demonstrated by the Perl's Prussian blue staining of

238   cells shown in Figure 2a; cancer cells appear pink, and the intracellular iron is blue. Labelling efficiency of

239   96.33±1.20% was achieved with 97.33±0.88% cell viability.

240

241   ***In Vivo* Studies**

242   ***Experimental Endpoint***

243   In our experience, intracardiac injection of 1.5×10^5 231BR cells in nude mice results in brain tumor burden,

244   significant weight loss and neurological impairments which leads to a requirement for euthanasia at 28-34 days post

245   injection. In this study the nude mice reached experimental endpoint on day 32. In contrast, NSG mice could only

246   be studied until day 21, at which time they had reached a weight loss greater than 15% of their body weight,

247   resulting in extreme cachexia and anorexia. Additionally, these mice showed severe signs of neurological

248   impairment, resulting in the inability to perform normal functions and exhibiting paralysis and circling. Post-mortem

249   examination also revealed significant liver tumor burden, which also contributed to the early, unexpected endpoint.

250

251   ***Imaging Cell Arrest and Retention***

252   On day 0, bSSFP brain images confirmed the successful intracardiac injection of MPIO-labeled cancer cells in all

253   mice; iron-labeled cancer cells appeared as distinct regions of signal void throughout the brain due to their initial

254   arrest in brain vasculature (Figure 2b). Figure 3a shows representative day 0 images for each mouse strain. When

255   quantifying the percentage of the brain consisting of black signal voids, approximately 4.69%±1.71 and 6.26%±1.86

256   of the brains of NSG and nude mice contained arrested cancer cells, respectively. At each strain's endpoint, the

257   number of black pixels was again determined, with percentages significantly reduced to approximately 1.89%±0.57

258   in NSG mice (day 21) and 2.45%±0.48 in nude mice (day 32). While the number of arrested cancer cells

259   significantly differs from day 0 to endpoint for both NSG ($p = 0.03$) and nude mice ($p = 0.02$), there was no

260   significant differences between strains at each time point (Figure 3b).

261

262   ***Day 21 MRI***

263   On day 21, metastases were detectable in bSSFP brain images as regions of signal hyperintensity in both strains of

264   mice (Figure 4a). On day 21, the mean number of MRI-detectable metastases was significantly higher in NSG mice

10

265   (63.70±5.37) compared to nude mice (15.33±4.29) (Figure 4b). While the nude mice had fewer tumors, they were

266   significantly larger. The mean volume of tumors in nude mice was 0.06 mm^3±0.01, compared to 0.04 mm^3±0.003

267   for NSG mice (Figure 4c). This mean volume was based on a total number of 637 tumors in all NSG mice and 72

268   tumors counted in all nude mice. At day 21, the mean tumor burden was significantly higher for NSG mice (2.39

269   mm^3±0.18) compared to nude mice (0.82 mm^3±0.35) (Figure 4D).

270

271   ***Day 32 MRI***

272   Nude mice were followed out their endpoint of day 32 and imaging analysis was compared to the endpoint data for

273   the NSG mice (Figure 5). The mean number and volume of brain metastases in nude mice increased between days

274   21 and 32. On day 32 the mean number of brain metastases in nude mice was 39.60±10.99. When comparing the

275   mean number of metastases for NSG and nude mice at their respective endpoints there was no longer a significant

276   difference (p = 0.07) (Figure 5b).

277   On day 32 the mean volume of brain metastases in nude mice was 0.32±0.23 mm^3, compared to 0.04±0.03 mm^3 on

278   day 21. This was significantly higher (p = <0.0001) than the mean volume of brain metastases at the NSG endpoint

279   (Figure 5c). Accordingly, nude mice had significantly more tumor burden than NSG mice (Figure 4d), which was a

280   reversal from the previous timepoint at day 21. Due to the earlier endpoint of NSG mice but lesser brain tumor

281   burden, body MRI was acquired for an NSG mouse at day 20. Notably, there was significant tumor burden detected

282   by MRI within the liver, lungs (Figure 6A), and lymph nodes (Figure 6b) of the NSG mice. Nude mice had no MRI-

283   detectable tumors within the body outside the brain (Figure 6c).

284

285   ***Ex Vivo Liver MRI***

286   Discrete signal voids were visible in the day 0 images of *ex vivo* livers from each strain of mouse, suggesting the

287   arrest of iron labeled 231BR cells throughout the liver (Figure 6d,e). Ex vivo liver mages obtained from mice at

288   endpoint showed numerous regions of abnormal high signal intensity associated with liver metastases, confirming

289   the *in vivo* image results (Figure 6f). A photo of a representative liver sample clearly shows the liver metastases on

290   the surface (Figure 6h). No regions of abnormal signal hyperintensity were observed in ex vivo images of the nude

291   mouse liver (6g). H&E stained sections of the liver tissue from NSG mice confirmed the presence of metastases (6i)

292   and ki67 staining showed that they were highly proliferative (6j).

11

293 **Discussion**

294 This work demonstrates for the first time the use of *in vivo* longitudinal MRI based cell tracking to compare murine

295 models of brain metastatic breast cancer. We show that there are significant differences in tumor progression for

296 231BR cells in NSG versus nude mice. While the initial arrest, clearance, and retention of iron-labeled cells was

297 similar, brain metastases developed more quickly in NSG mice and NSG mice developed substantial body tumor

298 burden, particularly in the liver, leading to an earlier endpoint.

299

300 The 231BR cell line was developed by Yoneda et al [15]. and is a brain-colonizing subline of the metastatic triple-

301 negative MDA-MB-231 human breast cancer cell line, which was isolated by six repeated cycles of intra-cardiac

302 injection and harvesting from brain metastases grown in nude mice. In our lab, the intra-cardiac injections are

303 performed using ultrasound (US) guidance. Of note, was our observation by US of a thicker heart muscle

304 surrounding the left ventricle of the NSG mouse. This anatomical observation made intracardiac injections more

305 difficult, as the ventricular space appeared smaller with US. The observation of signal voids in brain images

306 acquired on day 0 was used to identify successful delivery of cells to the brain. In this study, all mice imaged had

307 successful injections and were included in the study. Delivery of cells to a specific organ is related to the cardiac

308 output that is delivered to that organ. The cardiac output to the brain of a mouse is ~9.5% [38]. Here, we injected

309 150,000 cells into the left ventricle of the heart, and therefore we can expect ~14,250 cells to be successfully

310 delivered to the brain. Only a percentage of these cells will arrest; previous studies, however, have shown that less

311 than 1% of cells are retained in the microcirculation of the brain after 2 hours post-injection [38]. In previous

312 studies, we have used PPB staining and fluorescence microscopy to demonstrate that these signal voids correspond

313 to the presence of iron-labeled cells in the brain [35, 36].

314

315 The size of the signal void created by iron-labeled cells is much larger than the actual cell size, due to what is known

316 as the blooming effect. The blooming effect is a susceptibility artifact that occurs as a result of the iron oxide

317 nanoparticle, which causes a local magnetic field inhomogeneity [34]. We have previously shown that we can detect

318 single iron-labeled cells arrested in the mouse brain using cellular MRI [35, 39, 40]. Our image showed that the

319 number of signal voids in the brain was similar for nude and NSG mice on day 0 and at endpoint. While we

320 acknowledge that there is potential for immune cell uptake of the iron oxide nanoparticles that may be released by

12

321   dead cancer cells, we believe that the majority of the signal voids that remain present are live cancer cells retaining

322   iron. For example, in Parkins et al. [39] we investigated this mouse model using luciferase-positive 231BR cells and

323   measured a strong correlation on day 0 between the number of signal voids detected in day 0 brain MR images and

324   the brain signal measured in bioluminescence images, which is only detected from viable cells, providing evidence

325   that signal voids represent live iron-labeled cells. In Hamilton et al. [41] we used fluorescence activated cell sorting

326   (FACS) to successfully isolate live 231BR cells that were GFP-positive and labeled with red fluorescent (Flash Red)

327   MPIO from the brains of mice. The GFP+ Flash Red+ cells were collected and expanded *in vitro*. The majority

328   (~90%) of cells adhered to tissue culture plastic and successfully expanded, displaying the same cell morphology as

329   the original cultured 231BR cells. This provide additional support for our claim that signal voids in MRI represent

330   viable iron-positive cancer cells.

331   Our previous work has shown that the number of signal voids detected in MRI of the brain decreases over the course

332   of the experiment, from day 0 to day 8, which is expected as the large majority of cancer cells that arrest in the brain

333   do not survive and are cleared with time [39]. The signal voids which do persist in the brain over time are thought to

334   represent iron-retaining, non-proliferative or dormant cancer cells. These cells have been shown to contribute to

335   tumor recurrence [41]. It appears that both nude and NSG mice are capable of clearing dead cells from the brain.

336

337   3D MRI of the entire mouse brain at high resolution allowed us to view brain metastases in all 3 orientations and to

338   digitally re-slice images to carefully interrogate image data. We counted and measured the volume of all MRI-

339   detectable brain metastases. Brain metastases developed more quickly in NSG mice. At day 21 post cell injection

340   NSG mice had more than 3 times the number of brain metastases. The NK cells and the remaining innate immune

341   cells in nude mice likely contribute to the reduced tumor growth at this timepoint. This finding is in agreement with

342   the results of other groups that show that more immune compromised mouse models are more permissive for tumor

343   growth and metastasis [42-45]. Puchalapalli et al. [45] have previously reported an increase in the metastatic burden

344   (in liver, lungs, brain and bones) in NSG compared to nude mice that were injected with the parental 231 breast

345   cancer cell line in an intracardiac experimental metastasis model. In this study, metastases in each organ were

346   enumerated from *ex vivo* fluorescence microscopy images. Our work demonstrates the advantages of using *in vivo*

347   and longitudinal 3D MRI for the accounting of metastases in the whole brain.

348

13

349   NSG mice had to be euthanized at day 21/22. This was unexpected, as volumetric analyses of the tumor burden in

350   the brain at this timepoint compared to the tumor burden of the nude mice at their endpoint of day 32 indicated that

351   the NSG mice had lesser tumor burden in the brain. This suggested that there was a possibility of metastases to have

352   occurred elsewhere in the body that could be contributing to a greater disease burden. Mouse body MRI confirmed

353   tumors in the liver, lungs, and lymph nodes.

354

355   Nude mice were imaged at a third timepoint. On day 32 the number of brain metastases in nude mice was similar to

356   the number of brain metastases in NSG mice on day 21. The mean volume of the brain metastases in the nude mice

357   on day 32 was more than 3 times greater than those in NSG mice at day 21, having had more time to develop.

358   Overall, the brain tumor burden at necessary endpoint was significantly greater in nude mice.

359

360   *Ex vivo* images of livers removed on the day of the intracardiac injection of iron labeled 231BR cells revealed

361   numerous signal voids in all lobes of the liver in both strains of mice indicating that there was similar cancer cell

362   arrest for both strains at this timepoint. We did not do a quantitative analysis of liver signal voids, however, in a

363   previous study where we injected MPIO-labeled melanoma cells via the mesenteric vein, mouse livers were imaged

364   *ex vivo* by MRI and the signal void area was shown to correlate with the number of cells injected [46]. *Ex vivo*

365   images of livers removed at endpoint showed that numerous metastases formed in NSG mice while no liver

366   metastases could be detected in nude mice.

367   The 231BR cell line was developed to selectively grow distant metastases in the brains of nude mice, and so the

368   proliferation of metastases of this cell line in the liver demonstrates the loss of selectivity to the brain in the NSG

369   mouse.

370

371   **Conclusion**

372   In summary, high resolution cellular MRI allowed us to characterize the 231BR cell line in both the NSG and nude

373   mouse models. We found marked differences in tumor incidence, volumes, and body tumor burden between strains.

374   Our *in vivo* comprehensive analysis of cancer cell arrest, clearance, and tumor progression is important for

375   understanding the metastatic cascade of a model of breast cancer brain metastasis that can be challenging to obtain

376   with *in vitro* or *ex vivo* methods alone.

377

14

378 **List of Abbreviations**

379	**Abbreviations**	**Full Form**
380	bSSFP	balanced steady-state free precession
381	BW	bandwidth
382	DMEM	Dulbecco's modified Eagle's medium
383	FA	flip angle
384	FACS	fluorescence activated cell sorting
385	FIESTA	Fast Imaging Employing Steady State Acquisition
386	GFP	green fluorescent protein
387	H&E	hematoxylin and eosin
388	MPIO	micron-sized iron oxide particles
389	MRI	magnetic resonance imaging
390	NSG	NOD/SCID/ILIIrg-/-
391	PBS	Perl's Prussian Blue
392	PDX	patient-derived xenograft
393	RF	radiofrequency
394	TE	echo time
395	TR	repetition time
396	US	ultrasound
397	231BR	MDA-MB-231BR

398

399 **Declarations**

400 **Funding**

401 This study was supported by the Canadian Institute for Health Research (P.J. Foster) and the Breast Cancer Society

402 of Canada (N.N. Knier).

403

404 **Conflicts of interest/Competing interests**

405 The authors declare that they have no competing interests.

406

407 **Ethics approval**

408 Animals were cared for in accordance with the standards of the Canadian Council on Animal

409 Care, and under an approved protocol of the Western University's Council on Animal Care (2018-135).

410

411 **Consent to participate**

412 Not applicable

413

414 **Consent for publication**

415 Not applicable

416

417 **Availability of data and materials**

418 The datasets used and/or analysed during the current study are available from the corresponding author on

419 reasonable request.

420

421 **Code availability**

422 Not applicable

423

424 **Author's Contributions**

425 P.J.F. designed the experiments. N.N.K, P.J.F, and A.M.H conducted the experiments. N.N.K. analyzed the data.

426 N.N.K. and P.J.F. wrote the main manuscript text. All authors reviewed the manuscript.

16

430

References

1. Patanaphan V, Salazar OM, Risco R. Breast cancer: metastatic patterns and their prognosis. Southern medical journal. 1988;81(9):1109–1112.

2. Gavrilovic IT, Posner JB. Brain metastases: epidemiology and pathophysiology. Journal of neuro-oncology. 2005;75(1):5–14.

3. Nayak L, Lee EQ, Wen PY. Epidemiology of brain metastases. Current oncology reports. 2012;14(1):48–54.

4. Tabouret E, Chinot O, Metellus P, Tallet A, Viens P, Goncalves A. Recent trends in epidemiology of brain metastases: an overview. Anticancer research. 2012;32(11):4655–4662.

5. Anders C, Carey LA. Understanding and treating triple-negative breast cancer. Oncology (Williston Park, NY). 2008;22(11):1233.

6. Heitz F, Harter P, Lueck H-J, Fissler-Eckhoff A, Lorenz-Salehi F, Scheil-Bertram S, et al. Triple-negative and HER2-overexpressing breast cancers exhibit an elevated risk and an earlier occurrence of cerebral metastases. European journal of cancer. 2009;45(16):2792–2798.

7. Loibl S, Gianni L. HER2-positive breast cancer. The Lancet. 2017;389(10087):2415–2429.

8. Chambers AF, Groom AC, MacDonald IC. Dissemination and growth of cancer cells in metastatic sites. Nature Reviews Cancer. 2002;2(8):563–572.

9. Goss PE, Chambers AF. Does tumour dormancy offer a therapeutic target? Nature Reviews Cancer. 2010;10(12):871–877.

10. Fehm T, Mueller V, Marches R, Klein G, Gueckel B, Neubauer H, et al. Tumor cell dormancy: implications for the biology and treatment of breast cancer. Apmis. 2008;116(7–8):742–753.

11. Brackstone M, Townson JL, Chambers AF. Tumour dormancy in breast cancer: an update. Breast Cancer Research. 2007;9(3):208.

12. Lockman PR, Mittapalli RK, Taskar KS, Rudraraju V, Gril B, Bohn KA, et al. Heterogeneous blood–tumor barrier permeability determines drug efficacy in experimental brain metastases of breast cancer. Clinical cancer research. 2010;16(23):5664–5678.

13. Burdall SE, Hanby AM, Lansdown MR, Speirs V. Breast cancer cell lines: friend or foe? Breast cancer research. 2003;5(2):89.

14. Pelleitier M, Montplaisir S. The nude mouse: a model of deficient T-cell function. Methods and achievements in experimental pathology. 1975;7:149–166.

15. Yoneda T, Williams PJ, Hiraga T, Niewolna M, Nishimura R. A bone-seeking clone exhibits different biological properties from the MDA-MB-231 parental human breast cancer cells and a brain-seeking clone in vivo and in vitro. Journal of bone and mineral research. 2001;16(8):1486–1495.

16. Kumar S, Bajaj S, Bodla RB. Preclinical screening methods in cancer. Indian journal of pharmacology. 2016;48(5):481.

17. Gillet J-P, Varma S, Gottesman MM. The clinical relevance of cancer cell lines. Journal of the National Cancer Institute. 2013;105(7):452–458.

18

18. Siolas D, Hannon GJ. Patient-derived tumor xenografts: transforming clinical samples into mouse models. Cancer research. 2013;73(17):5315–5319.

19. Sulaiman A, Wang L. Bridging the divide: preclinical research discrepancies between triple-negative breast cancer cell lines and patient tumors. Oncotarget. 2017;8(68):113269.

20. Weeber F, Ooft SN, Dijkstra KK, Voest EE. Tumor organoids as a pre-clinical cancer model for drug discovery. Cell chemical biology. 2017;24(9):1092–1100.

21. Ruggeri BA, Camp F, Miknyoczki S. Animal models of disease: pre-clinical animal models of cancer and their applications and utility in drug discovery. Biochemical pharmacology. 2014;87(1):150–161.

22. Sharpless NE, DePinho RA. The mighty mouse: genetically engineered mouse models in cancer drug development. Nature reviews Drug discovery. 2006;5(9):741–754.

23. Dobrolecki LE, Airhart SD, Alferez DG, Aparicio S, Behbod F, Bentires-Alj M, et al. Patient-derived xenograft (PDX) models in basic and translational breast cancer research. Cancer and Metastasis Reviews. 2016;35(4):547–573.

24. Whittle JR, Lewis MT, Lindeman GJ, Visvader JE. Patient-derived xenograft models of breast cancer and their predictive power. Breast cancer research. 2015;17(1):17.

25. Jung J, Seol HS, Chang S. The generation and application of patient-derived xenograft model for cancer research. Cancer research and treatment: official journal of Korean Cancer Association. 2018;50(1):1.

26. Yu J, Qin B, Moyer AM, Sinnwell JP, Thompson KJ, Copland JA, et al. Establishing and characterizing patient-derived xenografts using pre-chemotherapy percutaneous biopsy and post-chemotherapy surgical samples from a prospective neoadjuvant breast cancer study. Breast Cancer Research. 2017;19(1):130.

27. Contreras-Zárate MJ, Ormond DR, Gillen AE, Hanna C, Day NL, Serkova NJ, et al. Development of novel patient-derived xenografts from breast cancer brain metastases. Frontiers in oncology. 2017;7:252.

28. Hoffmann J, Fichtner I, Lemm M, Lienau P, Hess-Stumpp H, Rotgeri A, et al. Sagopilone crosses the blood–brain barrier in vivo to inhibit brain tumor growth and metastases. Neuro-oncology. 2009;11(2):158–166.

29. Naumov GN, MacDonald IC, Weinmeister PM, Kerkvliet N, Nadkarni KV, Wilson SM, et al. Persistence of solitary mammary carcinoma cells in a secondary site: a possible contributor to dormancy. Cancer research. 2002;62(7):2162–2168.

30. Shafie SM, Grantham FH. Role of hormones in the growth and regression of human breast cancer cells (MCF-7) transplanted into athymic nude mice. Journal of the National Cancer Institute. 1981;67(1):51–56.

31. Murrell DH, Foster PJ, Chambers AF. Brain metastases from breast cancer: lessons from experimental magnetic resonance imaging studies and clinical implications. Journal of molecular medicine. 2014;92(1):5–12.

32. Foster-Gareau P, Heyn C, Alejski A, Rutt BK. Imaging single mammalian cells with a 1.5 T clinical MRI scanner. Magnetic Resonance in Medicine: An Official Journal of the International Society for Magnetic Resonance in Medicine. 2003;49(5):968–971.

33. McFadden C, Mallett CL, Foster PJ. Labeling of multiple cell lines using a new iron oxide agent for cell tracking by MRI. Contrast media & molecular imaging. 2011;6(6):514–522.

34. Makela AV, Murrell DH, Parkins KM, Kara J, Gaudet JM, Foster PJ. Cellular imaging with MRI. Topics in Magnetic Resonance Imaging. 2016;25(5):177–186.

35. Heyn C, Ronald JA, Ramadan SS, Snir JA, Barry AM, MacKenzie LT, et al. In vivo MRI of cancer cell fate at the single-cell level in a mouse model of breast cancer metastasis to the brain. Magnetic Resonance in Medicine: An Official Journal of the International Society for Magnetic Resonance in Medicine. 2006;56(5):1001–1010.

36. Murrell DH, Zarghami N, Jensen MD, Dickson F, Chambers AF, Wong E, et al. MRI surveillance of cancer cell fate in a brain metastasis model after early radiotherapy. Magnetic resonance in medicine. 2017;78(4):1506–1512.

37. Economopoulos V, Chen Y, McFadden C, Foster PJ. MRI detection of nonproliferative tumor cells in lymph node metastases using iron oxide particles in a mouse model of breast cancer. Translational oncology. 2013;6(3):347.

38. Basse P, Hokland P, Heron I, Hokland M. Fate of tumor cells injected into left ventricle of heart in BALB/c mice: role of natural killer cells. JNCI: Journal of the National Cancer Institute. 1988;80(9):657–665.

39. Parkins KM, Hamilton AM, Makela AV, Chen Y, Foster PJ, Ronald JA. A multimodality imaging model to track viable breast cancer cells from single arrest to metastasis in the mouse brain. Scientific reports. 2016;6(1):1–9.

40. Murrell DH, Hamilton AM, Mallett CL, van Gorkum R, Chambers AF, Foster PJ. Understanding heterogeneity and permeability of brain metastases in murine models of HER2-positive breast cancer through magnetic resonance imaging: implications for detection and therapy. Translational oncology. 2015;8(3):176–184.

41. Hamilton AM, Parkins KM, Murrell DH, Ronald JA, Foster PJ. Investigating the impact of a primary tumor on metastasis and dormancy using MRI: new insights into the mechanism of concomitant tumor resistance. Tomography. 2016;2(2):79.

42. Simpson-Abelson MR, Sonnenberg GF, Takita H, Yokota SJ, Conway TF, Kelleher RJ, et al. Long-term engraftment and expansion of tumor-derived memory T cells following the implantation of non-disrupted pieces of human lung tumor into NOD-scid IL2Rγnull mice. The Journal of Immunology. 2008;180(10):7009–7018.

43. Agliano A, Martin-Padura I, Mancuso P, Marighetti P, Rabascio C, Pruneri G, et al. Human acute leukemia cells injected in NOD/LtSz-scid/IL-2Rγ null mice generate a faster and more efficient disease compared to other NOD/scid-related strains. International journal of cancer. 2008;123(9):2222–2227.

44. Quintana E, Shackleton M, Sabel MS, Fullen DR, Johnson TM, Morrison SJ. Efficient tumour formation by single human melanoma cells. Nature. 2008;456(7222):593–598.

45. Puchalapalli M, Zeng X, Mu L, Anderson A, Glickman LH, Zhang M, et al. NSG mice provide a better spontaneous model of breast cancer metastasis than athymic (nude) mice. PLoS One. 2016;11(9).

46. Townson JL, Ramadan SS, Simedrea C, Rutt BK, MacDonald IC, Foster PJ, Chambers AF. Three-dimensional imaging and quantification of both solitary cells and metastases in whole mouse liver by magnetic resonance imaging. Cancer research. 2009 Nov 1;69(21):8326-31.
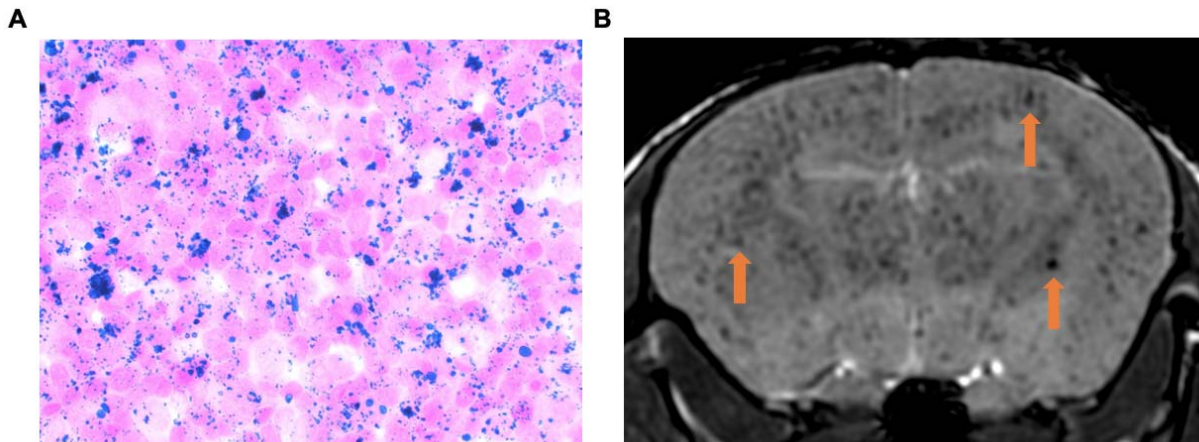
Figure 1
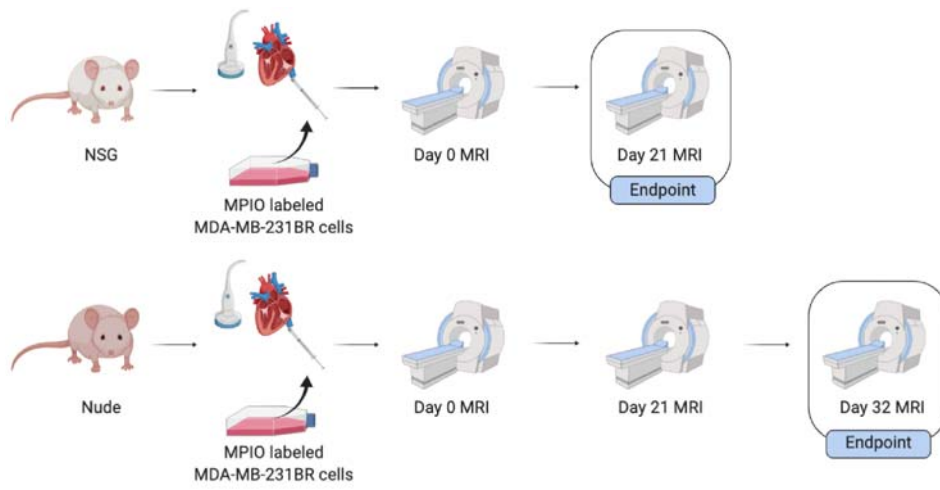
590

591   **Figure. 1 Experimental design for the NSG and nude mouse model**
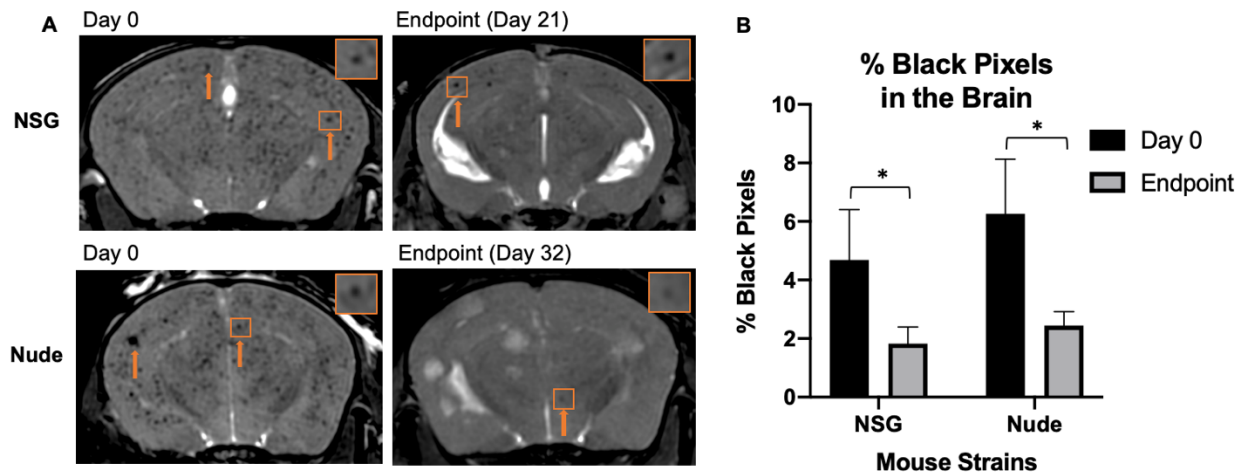
Figure 2

592

593 **Figure. 2 Iron labeling and injection of 231BR cells** (A) Perl's Prussian Blue stain showing intracellular iron

594 (blue, PPB) detected within MDA-MB-231BR cells (pink, Nuclear fast red) *in vitro*. (B) Representative day 0 image

595 showing visualization of successful iron-labeled cancer cell delivery by intracardiac injection as regions of signal

596 void (orange arrows)

Figure 3

597

598 **Figure. 3 Cancer cell arrest and clearance** (A) Balanced steady-state free precession images showing initial

599 cancer cell arrest at day 0 and clearance and retention at endpoint. The orange arrows indicate regions of signal void.

600 (B) The percentage of black pixels, representing regions of signal void was not significantly different between

601 strains, however there was a significant decrease within strains from day 0 to endpoint, suggesting similar cancer

602 cell arrest and clearance between nude and NOD/SCID/ILIIrg-/- mice
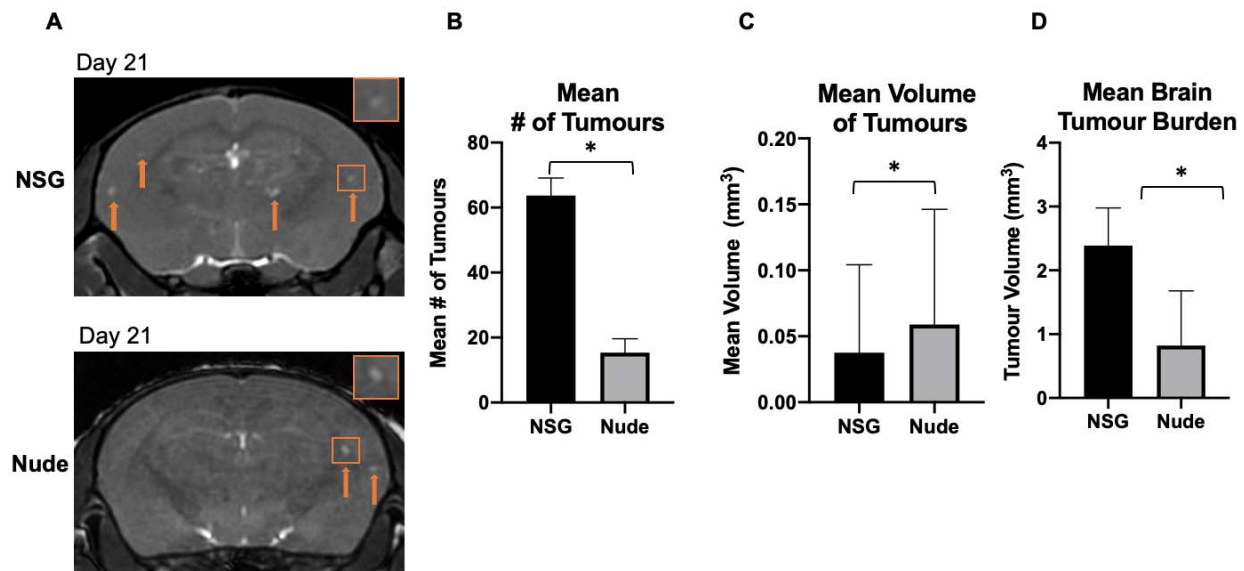
Figure 4

603

604 **Figure. 4 Day 21 visualization and quantification of brain metastases** (A) Balanced steady-state free precession

605 images showing brain metastases in both strains of mice as regions of signal hyperintensity (orange arrows) at day

606 21. (B) There were significantly more brain metastases on average detected with MRI in NSG mice than nude mice

607 at day 21. (C) The mean volume of tumors present in the brain was significantly greater in nude mice than NSGs.

608 (D) The brain tumor burden of NOD/SCID/ILIIrg-/- mice was significantly higher than in nude mice at day 21. Data

609 is presented as mean +/- SEM. *indicates $p < 0.05$

Figure 5
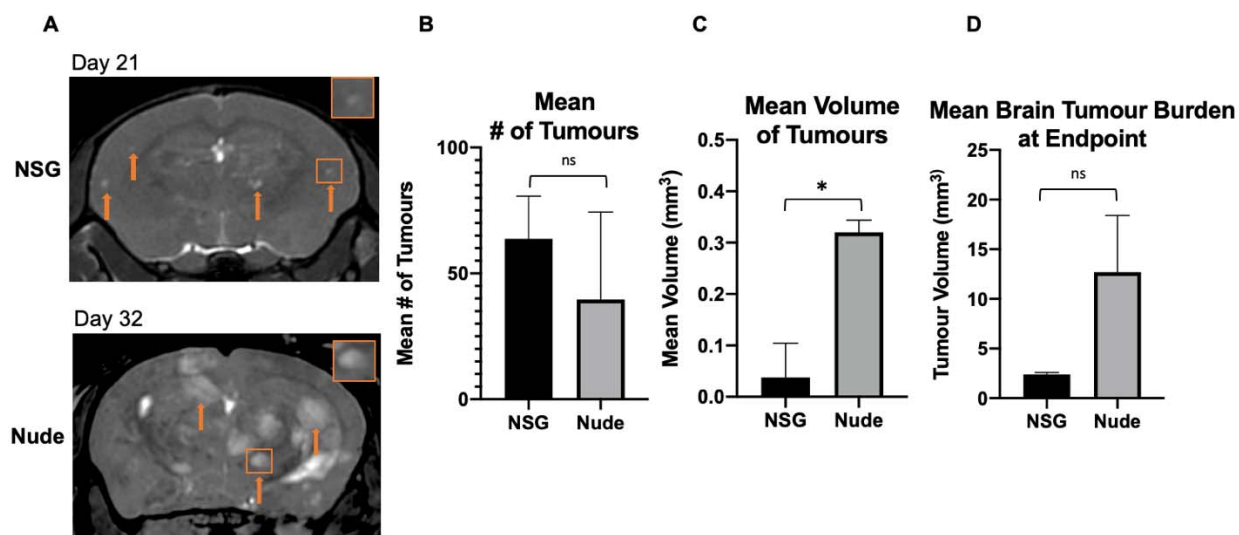
610

611   **Figure. 5 Endpoint visualization and quantification of brain metastases** (A) Magnetic resonance images of both

612   NOD/SCID/ILIIrg-/- and nude mice at each strain's respective endpoints (Day 21 for NOD/SCID/ILIIrg-/- , Day 32

613   for nude) showing regions of signal hyperintensity where brain metastases have developed (orange arrows). (B)

614   There was no significant difference between the number of brain metastases detected with magnetic resonance

615   imaging between strains at endpoint. (C) The tumors in the nude mice were significantly larger in volume than those

616   in the NOD/SCID/ILIIrg-/- mice. (D) The total tumor burden within the brain at endpoint in both nude and mice was

617   not significantly different. Data is presented as mean +/- SEM. *indicates $p < 0.05$

Figure 6
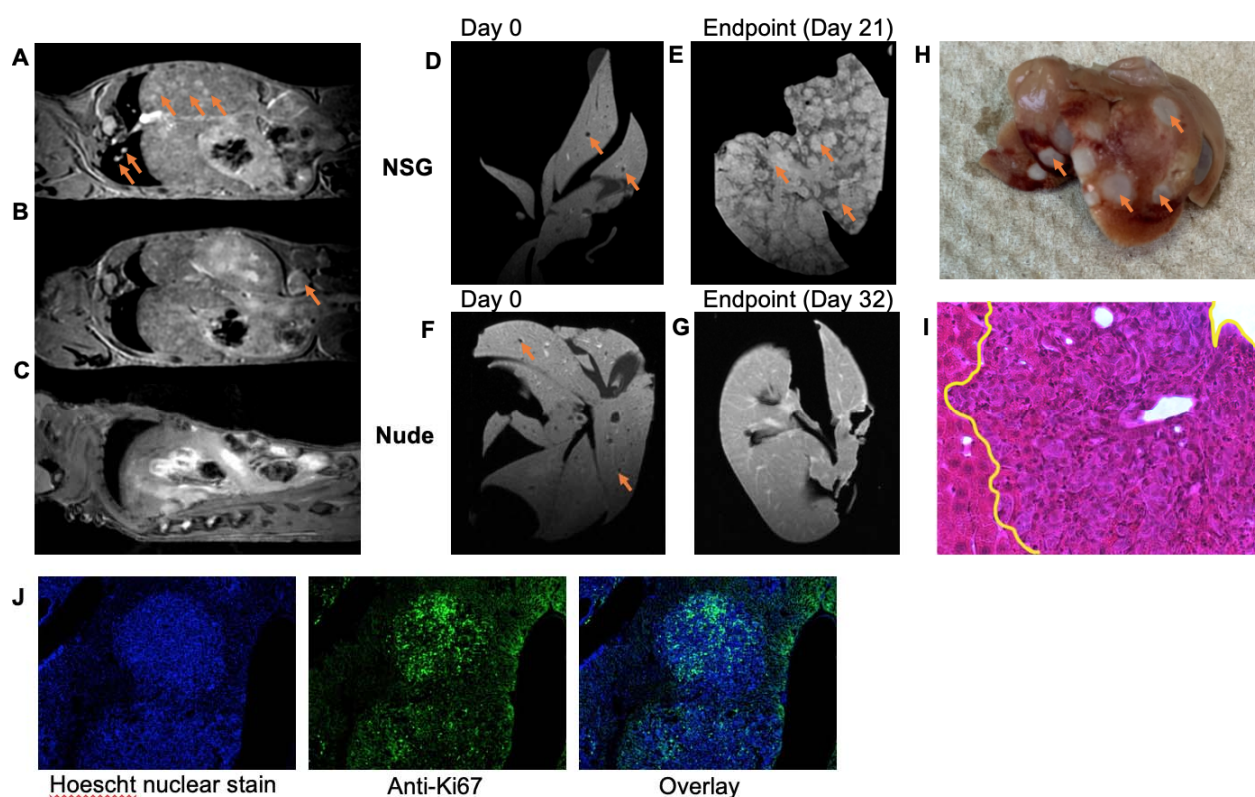
Figure. 6 Body and liver imaging with correlative histology and immunofluorescence (A) Body imaging of
NOD/SCID/ILIIrg-/- mouse allowed for detection of significant tumor burden in the liver, lungs. (B) Tumors were
detected in the lymph nodes of NOD/SCID/ILIIrg-/- mice with magnetic resonance imaging. (C) No tumors were
detected with magnetic resonance imaging in the nude mouse body. (D) Spoiled gradient echo sequence image
showing initial arrest of cancer cells in *ex vivo* liver at Day 0 for NOD/SCID/ILIIrg-/- mouse (E) Spoiled gradient
echo sequence image of *ex vivo* liver showing regions of hyperintensity where liver metastases have developed in
the NOD/SCID/ILIIrg-/- mouse. (F) Day 0 spoiled gradient echo sequence image of *ex vivo* liver of from a nude
mouse showing signal voids, representing arrested cancer cells. (G) Spoiled gradient echo sequence image of Day
32 (endpoint) *ex vivo* liver of a nude mouse with no magnetic resonance detectable metastases (H) Photo of a
representative *ex vivo* liver from an NOD/SCID/ILIIrg-/- mouse showing tumors on the exterior of the organ. (I)
H&E-stained section showing liver metastases that had developed in the NOD/SCID/ILIIrg-/- mouse (outlined in
yellow). (J) Ki67 staining showing a highly proliferative tumor within the NOD/SCID/ILIIrg-/- liver

26